

# JGR Solid Earth

## RESEARCH ARTICLE

10.1029/2021JB022144

### Key Points:

- N-S anisotropy and large XKS splitting times (~3 s) on the Indo-Burma Ranges are from trench parallel flow and lithospheric shortening
- XKS and local S results indicate trench-parallel flow and corner flow coexist in the mantle wedge beneath the Central Basin
- E-W oriented corner flow explains the splitting measurements in the Shan Plateau

### Supporting Information:

Supporting Information may be found in the online version of this article.

### Correspondence to:

Y. Ai and S. S. Gao,  
ysai@mail.iggcas.ac.cn;  
sgao@mst.edu

### Citation:

Fan, E., He, Y., Ai, Y., Gao, S. S., Liu, K. H., Jiang, M., et al. (2021). Seismic anisotropy and mantle flow constrained by shear wave splitting in central Myanmar. *Journal of Geophysical Research: Solid Earth*, 126, e2021JB022144. <https://doi.org/10.1029/2021JB022144>

Received 31 MAR 2021

Accepted 15 SEP 2021

## Seismic Anisotropy and Mantle Flow Constrained by Shear Wave Splitting in Central Myanmar

Enbo Fan<sup>1,2,3</sup> , Yumei He<sup>1,3,4</sup> , Yinshuang Ai<sup>1,3,4</sup> , Stephen S. Gao<sup>2</sup> , Kelly H. Liu<sup>2</sup> , Mingming Jiang<sup>1,3,4</sup> , Guangbing Hou<sup>1</sup>, Chit Thet Mon<sup>1,5</sup>, Myo Thant<sup>6</sup>, and Kyaing Sein<sup>7</sup>

<sup>1</sup>Key Laboratory of Earth and Planetary Physics, Institute of Geology and Geophysics, Chinese Academy of Sciences, Beijing, China, <sup>2</sup>Geology and Geophysics Program, Missouri University of Science and Technology, Rolla, MO, USA, <sup>3</sup>College of Earth and Planetary Sciences, University of Chinese Academy of Sciences, Beijing, China, <sup>4</sup>Innovation Academy for Earth Science, Chinese Academy of Sciences, Beijing, China, <sup>5</sup>Department of Geology, Dagon University, Yangon, Myanmar, <sup>6</sup>Department of Geology, University of Yangon, Yangon, Myanmar, <sup>7</sup>Myanmar Geosciences Society, Yangon, Myanmar

**Abstract** This study represents the first campaign-style teleseismic shear wave splitting (SWS) investigation of central Myanmar, an area that is tectonically controlled by the oblique subduction of the Indian Plate underneath the Eurasian Plate. The resulting 678 well-defined and 247 null SWS measurements obtained from recently deployed 71 broadband seismic stations show that the Indo-Burma Ranges (IBR) possess mostly N-S fast orientations that are parallel to the trend of the depth contours of the subducted slab. Relative to the global average of 1.0 s, extremely large splitting times with station-averaged values ranging from 1.28 to 2.79 s and an area-averaged value of  $2.09 \pm 0.55$  s are observed in the IBR. In contrast, the Central Basin (CB) and the Shan Plateau (SP) are characterized by slightly larger than normal splitting times. The fast orientations observed in the CB are mostly NE-SW in the northern part of the study area, N-S in the central part, and NW-SE in the southern part. The fast orientations change from nearly N-S along the N-S oriented Sagaing Fault, to NW-SE in the central and eastern portions of the SP. These observations, together with SWS measurements using local S events, crustal anisotropy measurements using P-to-S receiver functions, and the estimated depth of the source of anisotropy using the spatial coherency of the splitting parameters, suggest the presence of a trench-parallel sub-slab flow system driven by slab rollback, a trench-perpendicular corner flow, and a trench-parallel flow possibly entering the mantle wedge through a slab window or gap.

**Plain Language Summary** Myanmar is located at the boundary between the Indian Plate and the Eurasian Plate. Here, the Indian Plate moves northward at a rate that is faster than most other tectonic plates on Earth and subducts obliquely beneath the Eurasian Plate. This subduction not only causes a strong deformation of the Earth's surface, forming the approximately 1,250 km long, N-S trending Indo-Burma Ranges, but also results in pervasive crustal deformation and possibly modulates the mantle flow field in the area. Mostly due to the limited coverage by broadband seismic stations until recently, crustal deformation and mantle flow beneath Myanmar were poorly understood. In this study, we used data from 71 seismic stations that we deployed in central Myanmar to analyze seismic azimuthal anisotropy, that is, the directional dependence of the velocity of seismic waves in a medium, at different depths. Based on the established relationship between seismic anisotropy and mantle flow, we proposed a model to explain the observations. Our model implies the presence of a trench-parallel mantle flow beneath the subducted Indian Plate. Above the plate, there are two flow systems with trench-parallel and trench-orthogonal orientations, respectively, with spatially varying strengths.

## 1. Introduction

The central Myanmar region is the southward extension of the Tibetan Plateau through the Eastern Himalayan Syntaxis and is largely situated above the obliquely subducting Indian slab beneath the Eurasian Plate (Figure 1). At present, the Indian Plate moves at a direction of about N50°E in a no-net-rotation reference frame based on the NNR-MORVEL56 model (Argus et al., 2011), with a convergence rate of 13–17 mm/yr (Steckler et al., 2016) or 12–24 mm/yr (Mallick et al., 2019) relative to the Eurasian Plate in Myanmar. The

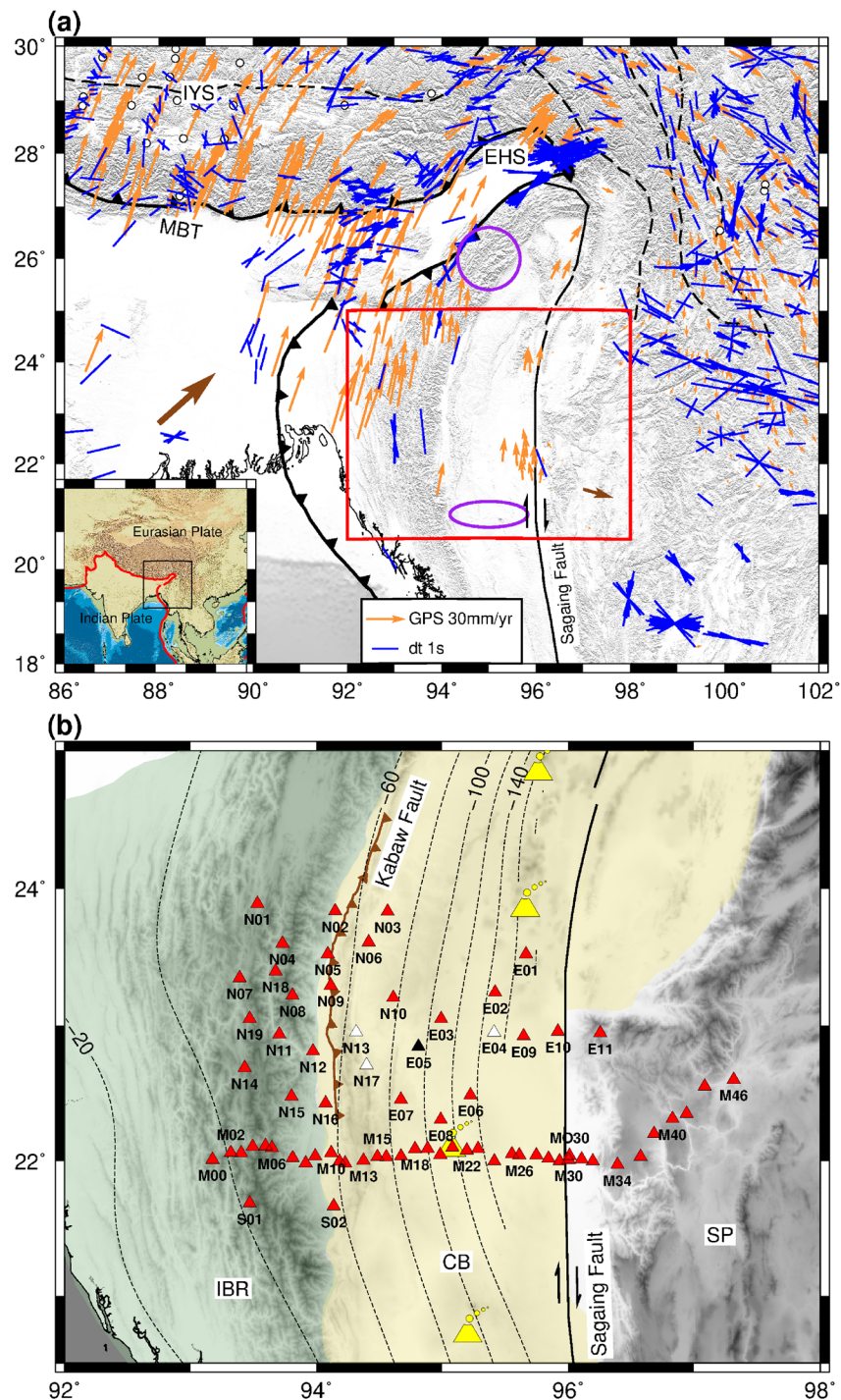


Figure 1.

active tectonics of central Myanmar is mainly controlled by two geodynamic processes. The first is shearing primarily originated from the obliqueness of the subduction, resulting in a series of approximately N-S oriented dextral strike-slip faults including the ~1,200 km long Sagaing Fault (SF), which links the Eastern Himalayan Syntaxis to the north and the Andaman Sea spreading center to the south (Sloan et al., 2017). The second is E-W oriented compression due to the coupling between the subducting Indian Plate and overriding Eurasian Plate that led to the formation of the Indo-Burma Ranges (IBR), which is interpreted as a wide accretionary wedge associated with the plate subduction since about 43 Ma (Rangin, 2017). The

Central Basin (CB), comprising Mesozoic and Cenozoic magmatic rocks, is interpreted as a combination of the forearc and back-arc basins that are separated by the Central Volcanic Arc Belt approximately along the basin axis (Rangin, 2017). The Shan Plateau (SP), which is separated from the CB by the SF, is covered by sedimentary rock sequences with ages ranging from the Precambrian to the Mesozoic (Curry, 2005; Mitchell, 1989).

While the Wadati-Benioff zone extends to a maximum depth of  $\sim 150$  km (Frohlich, 2006; Hurukawa et al., 2012), most seismic tomography studies suggest a greater depth extent of the slab, ranging from  $\sim 300$  km (Li et al., 2008) to the bottom of the mantle transition zone (Koulakov, 2011; Yao et al., 2021). Additionally, the tomography results of Raouf et al. (2017) suggest that the subducted part of the Indian lithosphere beneath the IBR at  $\sim 26^\circ\text{N}$  appears to have broken off from the rest, leaving a gap between the two segments in the depth range of  $\sim 50$ – $100$  km. Moreover, a recent receiver function (RF) study (Bai et al., 2020) using teleseismic data recorded by the same stations used in this study suggests the presence of a slab tear located approximately at  $21^\circ\text{N}$ . Previous studies (R. Hall & Morley, 2004; Kundu & Gahalaut, 2012; Lee et al., 2016; Li et al., 2008) suggest a westward trench migration and rollback of the subducting Indian slab, which can modulate the mantle flow system in the vicinity of the subduction zone (e.g., Long & Silver, 2008). Specifically, a trench-parallel asthenospheric flow in the sub-slab region produced by slab rollback is suggested by numerical modeling studies (e.g., Becker & Faccenna, 2009). Investigation of the mantle flow field in this complex system has the potential to shed light on the mantle dynamics and the relationship between surface dynamic processes and mantle deformation associated with plate subduction.

One of the most robust and commonly employed techniques for delineating crustal and mantle flow and deformation is shear wave splitting (SWS) analysis (Ando et al., 1980; Silver & Chan, 1991). SWS is the process whereby a shear wave splits into two quasi-S-waves with orthogonal polarization directions as it passes through a transversely isotropic medium, which is the simplest form of azimuthal anisotropy. The two waves travel at different speeds in the medium and therefore accumulate a separation between their arrivals. The splitting parameters include the polarization orientation of the fast wave which is termed as the fast orientation (or  $\phi$ ), and the delay time (splitting time or  $\delta t$ ) between those two components which is proportional to the product of the length of the path through the anisotropic material and the strength of the anisotropy. The most significant anisotropic domain within the Earth is the upper mantle, in which olivine, an anisotropic mineral, is the most abundant constituent. Laboratory experiments show that progressive simple shear (deformation) can lead to the development of lattice preferred orientations (LPO) of olivine minerals (e.g., Karato et al., 2008) and gradient in mantle flow velocity, with the fast orientation aligning with the mantle flow direction for A-, C-, and E-type olivine fabrics (Karato et al., 2008). Under conditions that are typically found near the tip of the mantle wedge above a subducted oceanic slab, including low-temperature, high pressure, and moderate water content, B-type olivine fabric could develop for which the fast orientation is perpendicular to the mantle flow direction (Jung & Karato, 2001; McCormack et al., 2013). Because the subducted slab is believed to be a water-poor continental lithosphere (Zheng et al., 2020), B-type olivine fabric is unlikely to be pervasively present in the area.

Due to the lack of sufficient coverage by broadband seismic stations, XKS (including SKS, SKKS, and PKS) splitting parameters were only measured at a few stations in the Myanmar region (L. Liu et al., 2019; Saikia et al., 2018). Most of them are in the IBR and one is near the SF. The fast orientations in the IBR follow the strike of the orogen and are interpreted as resulting from both the lithospheric deformation and asthenospheric flow (L. Liu et al., 2019; Saikia et al., 2018). Russo (2012) obtained 103 source-side splitting

**Figure 1.** (a) Topographic map of Myanmar and adjacent areas showing major tectonic provinces and previous well-defined PKS, SKKS, and SKS shear wave splitting measurements (blue bars) and null measurements (open circles) obtained from <http://splitting.gm.univ-montp2.fr/DB/public/searchdatabase.html> and Liu et al. (2019). Orange arrows represent GPS velocity measurements relative to Eurasia (M. Wang & Shen, 2020). Brown arrows show the directions of the absolute plate motion based on the NNR-MORVEL56 model (Argus et al., 2011). Major faults and plate boundaries were plotted as black and red curves in the main and inset figures, respectively (Y. Wang et al., 2014). Suture zones were plotted as dashed black lines. The purple circle at  $26^\circ\text{N}$  and the purple ellipse at  $21^\circ\text{N}$  mark the slab gap (Raouf et al., 2017) and slab tear (Bai et al., 2020), respectively. The mapped area is outlined by a black rectangle in the inset map. (b) Distribution of the 71 portable broadband stations. The red triangles indicate the 67 stations at which well-defined splitting parameters were obtained from this study, the white triangles indicate the three stations that obtained only null measurements, and the black triangle indicates the station with no reliable results. The tectonic units were delimited by different colors. Contours show the depth of the subducting Indian slab (Hayes et al., 2018). The yellow symbols mark the locations of magmatic rocks. The brown curve is the Kabaw Fault, and the black curve is the dextral Sagaing Fault. Central Basin (CB); Eastern Himalayan Syntaxis (EHS); Indo-Burma Ranges (IBR); Indus-Yalu Suture (IYS); Main Boundary Thrust (MBT); Shan Plateau (SP).

measurements from 15 earthquakes along the subducting slab that have been corrected for anisotropy beneath the receiver to study sub-slab anisotropy. The IBR shows predominantly trench-parallel fast orientations and the fast orientations in the CB are mostly trench-normal between latitude 22°N and 25°N. The splitting times have a mean of 3.0 s. The SWS measurements are attributed to mantle flow through a slab gap at 22°N and around the slab.

To gain insights into the previously poorly-understood mantle dynamics and deformation characteristics of the plate boundary system beneath central Myanmar, we deployed the first portable seismic array in Myanmar as part of the China-Myanmar Geophysical Survey of the Myanmar Orogen (CMGSMO) project. Here, we apply the SWS technique to both XKS and local S-waves, and combine the splitting measurements with observations of crustal anisotropy using P-to-S conversions at the Moho, to investigate the spatial distribution of anisotropy beneath central Myanmar and estimate the depth of anisotropy using the spatial coherency approach (K. H. Liu & Gao, 2011). A geodynamic model involving flow systems associated with trench migration and slab rollback is proposed to explain the observed azimuthal anisotropy in this tectonically complex area dominated by plate convergence.

## 2. Data and Methods

### 2.1. Data

We investigated SWS at 71 broadband seismic stations located throughout the IBR, the CB, and the SP (Figure 1). Thirty-nine stations (those with names starting with the letter “M” in Figure 1b) form a dense east-west trending linear subarray approximately along the 22°N latitudinal line, with spacings of 10–15 km. The other stations, which are 30–50 km apart, form a 2D backbone network. The stations were in operation from June 2016 to February 2018 (Mon et al., 2020), with a recording frequency of 40 samples per second. Each of the stations was equipped with either a Nanometrics Trillium 120PA or a Guralp CMG-3ESP broadband seismometer, together with a Reftek RT130 digitizer. Three kinds of P-to-S converted phases at the core-mantle boundary, including PKS, SKKS, and SKS, from earthquakes in the epicentral distance range between 84° and 180°, were utilized (Figure 2). We apply a cutoff magnitude of 5.6 for events with focal depths shallower than 100 km, and 5.5 for deeper events.

### 2.2. Methods

SWS analysis was performed by following the set of procedures and criteria described in K. H. Liu and Gao (2013). The XKS seismograms were band-pass filtered in the frequency band of 0.04–0.5 Hz, which includes the main XKS energy. The XKS time window used to compute the splitting parameters was initially set as 5 s before and 20 s after the predicted XKS arrival times computed based on the IASP91 Earth model. If the signal-to-noise ratio (SNR) on the radial component is smaller than 4.0, the event-station pair was not used. Details for computing the SNR can be found in K. H. Liu et al. (2008).

The remaining seismograms were then used to search for the optimal pair of XKS splitting parameters, which correspond to the minimum energy on the corrected transverse component (Silver & Chan, 1991). Manual checking was applied to each of the measurements, and if necessary, the XKS time window and the band-pass filtering parameters were adjusted to minimize the influence of non-XKS arrivals to the resulting optimal splitting parameters, whose standard deviation was estimated using the F-test described in Silver and Chan (1991). Only measurements with standard deviations less than 15° and 0.5 s, respectively, for  $\phi$  and  $\delta t$ , were kept.

The resulting measurements were ranked into A (outstanding), B (good), C (poor), and N (null) based on the similarity between the resultant fast and slow components, the uniqueness of the minimal energy point on the corrected transverse component, and the linearity of the horizontal particle motion pattern following the correction for splitting (K. H. Liu & Gao, 2013; K. H. Liu et al., 2008). Null measurements were also recorded in this study, for which we required a clearly visible XKS phase on the radial component and unobservable XKS energy on the original transverse component. Examples of well-constrained splitting measurements are shown in Figure 3.

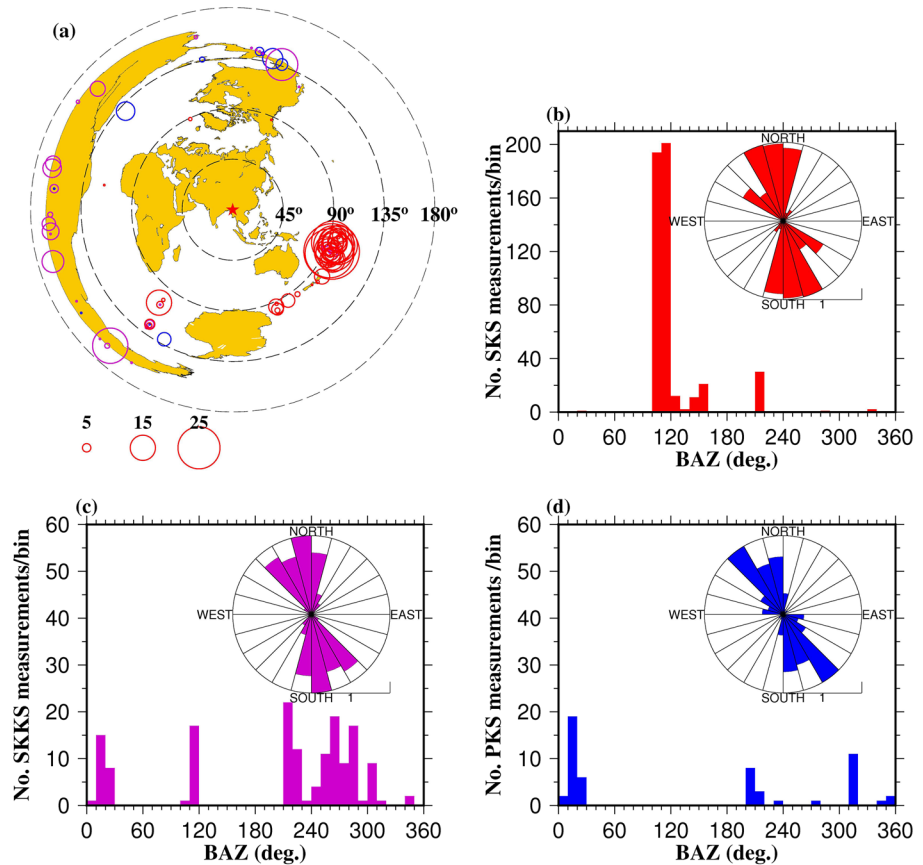


**Figure 2.** (a) Azimuthal equidistant projection map centered at the study area (star), showing the distribution of teleseismic events (circles) used in this study. The size of the circles is proportional to the number of shear wave splitting measurements from each event. Blue: PKS; Purple: SKKS; Red: SKS. (b) A histogram and a rose diagram illustrating the distributions of back-azimuths and resulting fast orientations of SKS measurements, respectively. (c) Same as (b), but for SKKS measurements. (d) Same as (b), but for PKS measurements.

To provide constraints on the vertical distribution of the observed anisotropy from XKS splitting, which is a measure of the integrated anisotropy from the core-mantle boundary to the surface, we applied three techniques in addition to XKS splitting to the data set. The first is estimating the depth of the main source of the observed anisotropy using the spatial coherency of the splitting parameters (K. H. Liu & Gao, 2011). The technique assumes an array of candidate depths and calculates a variation factor defined by Equation 7 in K. H. Liu and Gao (2011) at each depth. The weighting factors for the two parameters were chosen based on the maximum possible range of fast orientations and splitting times, as described in K. H. Liu and Gao (2011). The optimal depth corresponds to the maximum spatial coherency (or minimum spatial variation). Reliable application of this technique requires spatially varying single layer anisotropy with a constant depth, as detailed in K. H. Liu and Gao (2011). The second technique is to measure the contribution of the crust to the observed XKS splitting using the arrival time and amplitude of the source-normalized P-to-S converted phases (or RFs) from the Moho. A detailed description of the approach and its application to the southeastern Tibetan Plateau can be found in Kong et al. (2016). The third technique is to measure anisotropy from the focus of a local earthquake to the surface (e.g., Crampin & Booth, 1985). The optimal pair of splitting parameters is found by minimizing the lesser of the two eigenvalues of the covariance matrix of the corrected seismograms (Silver & Chan, 1991). Because this study is focused on XKS splitting, local splitting and RF analysis results from only a few critically-positioned stations that can provide constraints on the depth distribution of the observed XKS splitting are presented. Full analyses of the entire data set using both local SWS and RF analyses are the subjects of future studies.

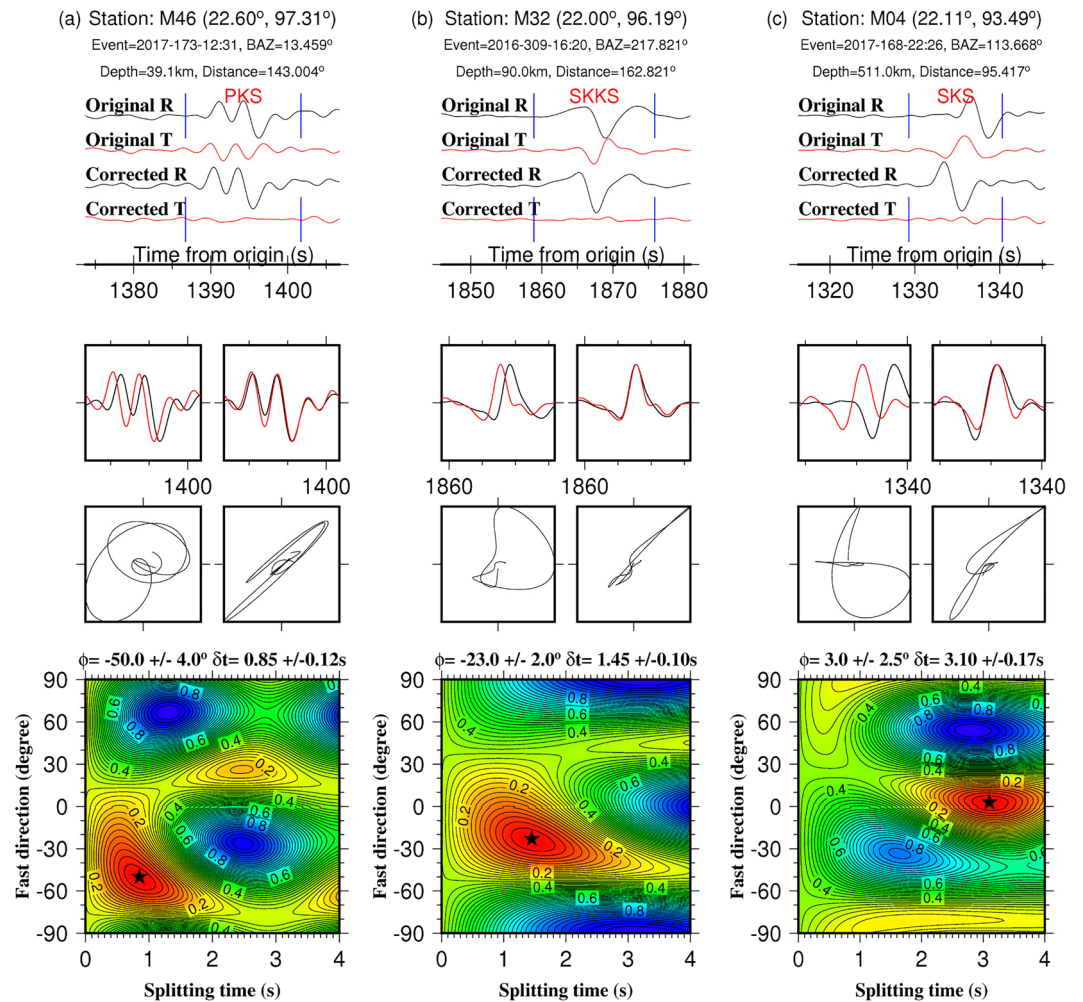


**Figure 3.** Examples of well-constrained PKS, SKKS, and SKS shear wave splitting measurements from Stations (a) M46, (b) M32, and (c) M04, respectively. Note the very large and well-constrained splitting time obtained at Station M04. For each measurement, showing the (top) original and corrected radial and transverse components, (middle) fast (red) and slow (black) waveforms and the associated particle motion pattern in the E-N plane, that is, N-S is along the y axis and E-W is along the x axis, (left) before and (right) after time delay correction, and (bottom) a contour map representing the normalized energy on the corrected transverse component in the XKS time window. The star indicates the optimal pair of splitting parameters corresponding to the minimum transverse energy.

### 3. Results

Among the 71 stations, well-defined (Quality A or B) measurements were obtained at 67 stations, three stations only produced null measurements, and one station did not result in any well-defined or null measurements. We obtained a total of 678 pairs of Quality A or B XKS parameters from 82 events (Figure 2a), including 54 PKS, 149 SKKS, and 475 SKS measurements (Figures 2b–2d). A total of 247 pairs of null measurements were obtained from 71 events (Figure S1), including 4 PKS, 75 SKKS, and 168 SKS measurements. The original and corrected radial and transverse components and the particle motion diagram for each of the 678 measurements (similar to Figure 3), and the splitting parameters plotted against the back azimuth for all the 67 stations can be found at [ftp://159.226.119.161/data/CMGSMO-1/SWSDData/web\\_XKS/all/web\\_XKS.html](ftp://159.226.119.161/data/CMGSMO-1/SWSDData/web_XKS/all/web_XKS.html) (Internet Explorer is recommended to open the link).

To investigate the existence of multilayered anisotropy which is characterized by splitting parameters varying as functions of the initial polarization (or back azimuth) with a  $\pi/2$  period (Rümpker & Silver, 1998; Silver & Savage, 1994), we plotted the individual splitting parameters against the back azimuth for each of the stations (see e.g., Figures 4 and S2) and visually verified the existence or non-existence of periodic

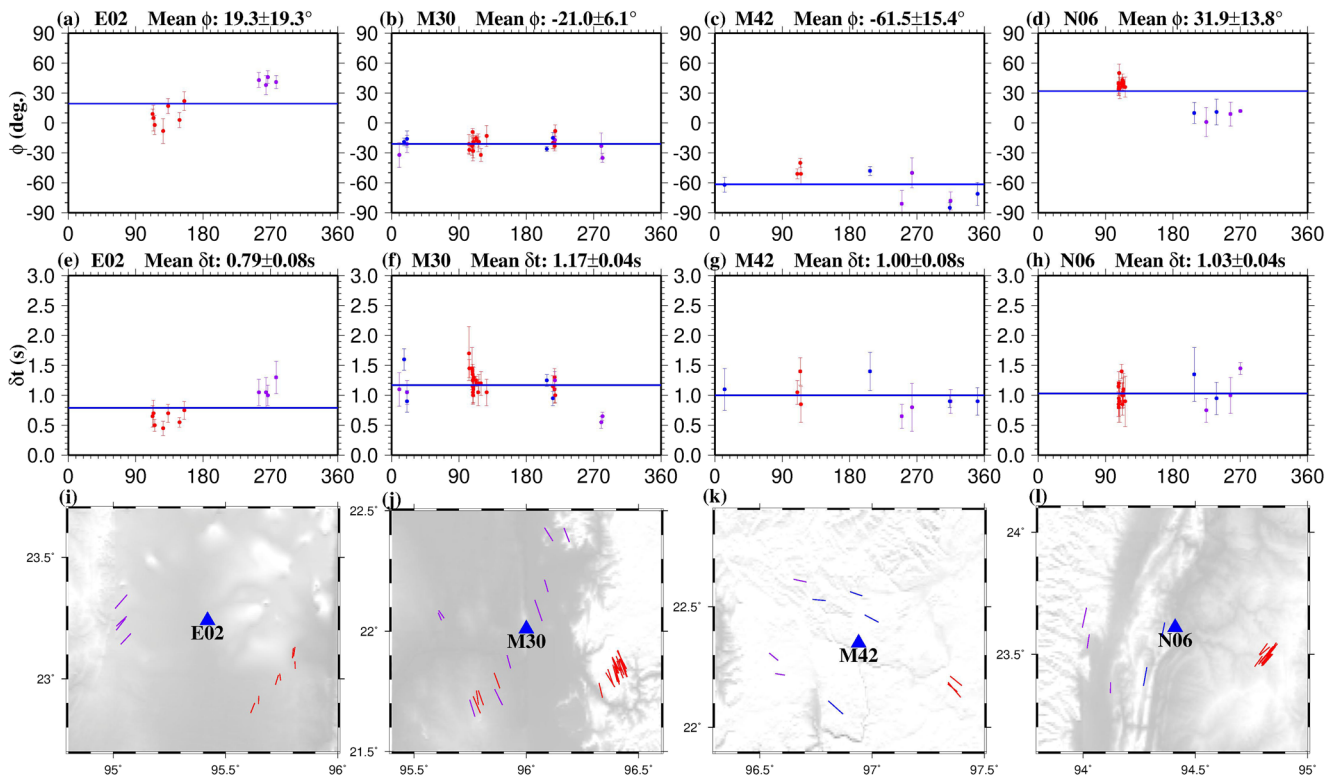


**Figure 4.** (a–d) XKS fast orientations for stations E02, M30, M42, and N06 plotted against back azimuth. (e–h) Same as (a–d) but for splitting times. (i–l) XKS splitting parameters from the 4 stations plotted above the ray-piercing points at 200 km deep on a topographic map. The blue triangles in (i–l) display the station locations, and the blue lines in (a–h) indicate the station-averaged values. The red, purple, and blue symbols represent results from the SKS, SKKS, and PKS phases, respectively.

azimuthal variations of the splitting parameters. For stations located in the boundary zone between neighboring areas with different splitting parameters (e.g., Stations E02 and N06 in Figure 4), the splitting parameters vary as functions of the ray piercing point location, suggesting that ray paths from different azimuths sample areas with different splitting parameters (K. H. Liu & Gao, 2013). Periodic azimuthal variations are not convincingly observed at any of the stations (e.g., Stations M30 and M42 in Figure 4), suggesting that a single layer of anisotropy with a horizontal axis of symmetry is sufficient to explain the observations. However, it must be mentioned that the azimuthal coverage at some of the stations is not sufficient to completely reject the possibility of systematic azimuthal variations of the splitting parameters, and consequently, the existence of complex anisotropy cannot be entirely ruled out.

For the entire study area, the resulting fast orientations are dominantly NNW-SSE with a circular mean of  $-15.3 \pm 25.3^\circ$ . No systematic differences between the results of SKS, SKKS, and PKS phases are observed (Figure 2), and the spatial variations are mainly controlled by the location of the ray-piercing points (Figure 5a).

In the IBR, we observed nearly consistent N-S fast orientations that are parallel to the strike of the orogen and also to the trend of the depth contours of the subducting slab. The corresponding splitting times have a mean value of  $2.09 \pm 0.55$  s, which is much greater than the global average of 1.0 s for continents (Silver, 1996). Among all the stations, the maximum splitting time is found at Station M04, which displays an average value of  $2.79 \pm 0.09$  s (Figure S2) and a maximum value that is greater than 3.0 s (Figure 3c), a value that is rarely matched by any reliable XKS splitting measurements in previous studies.

The splitting measurements in the CB show more spatial variability than the IBR and the splitting times reduce to  $\sim 1.0$  s from about  $\sim 2.0$  s across the IBR/CB boundary (Figure 5d), with a mean value of  $1.12 \pm 0.39$  s. Most of the fast orientations south of latitude  $22.2^\circ\text{N}$  are NW-SE, with a mean value of  $-30.7 \pm 25.2^\circ$ . In comparison, those in the area to the north of this latitude are mostly NE-SW, with a mean of  $34.6 \pm 33.7^\circ$ ,

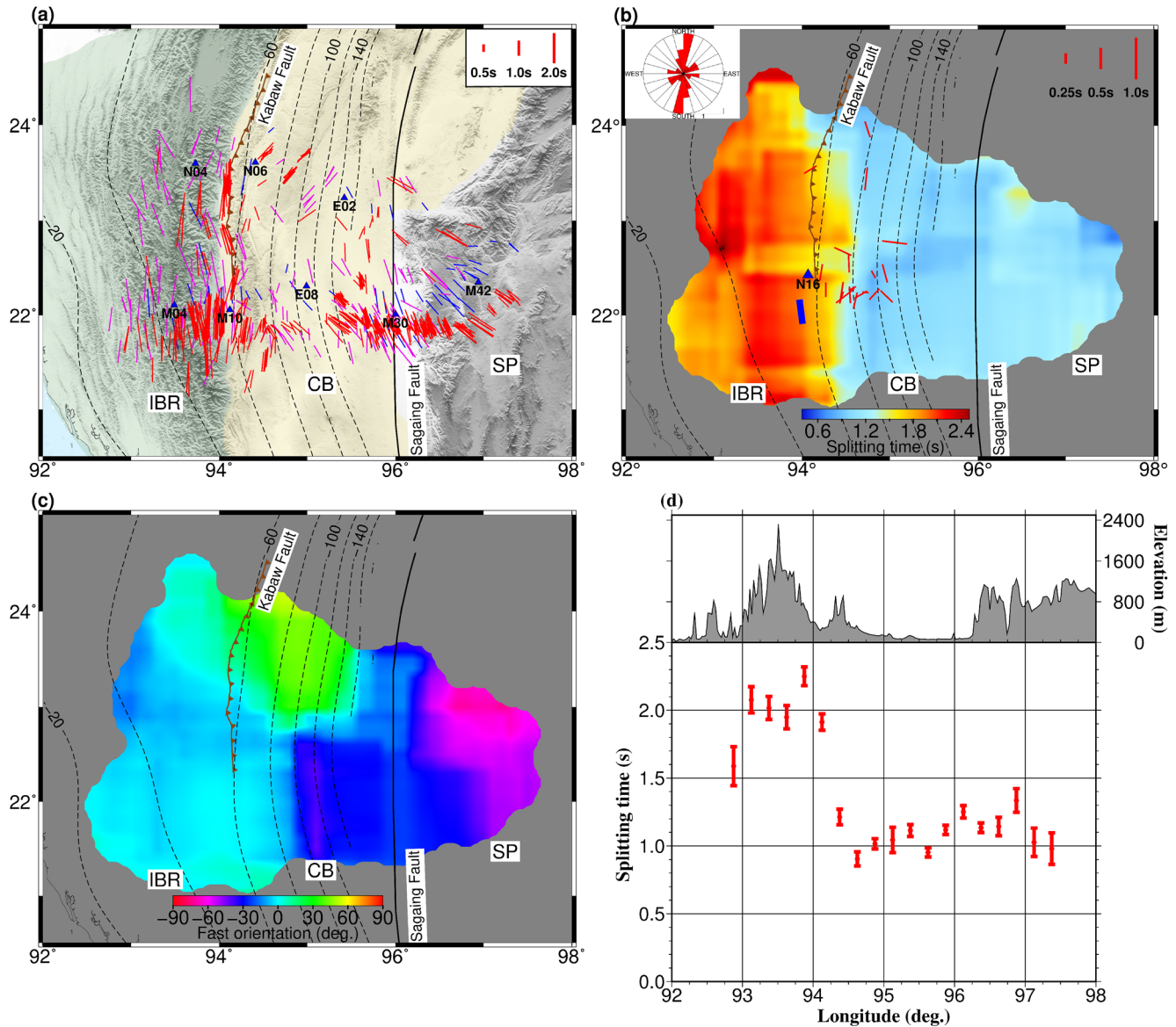


**Figure 5.** (a) Shear wave splitting measurements (colored bars) from this study plotted on a topographic map. The tectonic units are delimited by different colors. Contours show the depth of the subducting Indian slab (Hayes et al., 2018). Individual measurements from SKS, SKKS, and PKS are shown in red, purple, and blue, respectively, and are plotted above the ray-piercing points at 200 km deep. The eight stations discussed in the text are shown as blue triangles. For the other labels, see Figure 1. (b) Well-defined local S splitting measurements plotted at the midpoint between the events and stations. The ray paths are shown in Figure S6. The thick blue bar is a Pms splitting measurement at station M09. The rose diagram in the upper left corner illuminates the distribution of the resulting fast orientations of the local S measurements. The background color denotes the splitting time produced by averaging the XKS individual splitting times at the piercing points of 200 km deep in overlapping  $1^\circ \times 1^\circ$  blocks with a moving step of  $0.1^\circ$ . (c) Spatially averaged XKS fast orientations from individual measurements in each of the  $r = 0.4^\circ$  circles. (d) Averaged XKS splitting times over longitudinal bands of  $0.25^\circ$  wide (bottom panel) and surface elevation along latitude =  $21.9^\circ\text{N}$  (upper panel).

and most of the fast orientations in a narrow zone centered at this latitude are N-S. Interestingly, the contour lines of the subducted slab (Hayes et al., 2018) also demonstrate a directional change across this latitude, from NNW-SSE in the south to NNE-SSW in the north (Figure 5a).

The fast orientations observed in the SP show a counter-clockwise rotation toward the east, from nearly N-S along the SF which is the western boundary of the SP, to NW-SE and WNW-ESE in the central and eastern portions of this region (Figure 5c). There is no significant change in the splitting times observed in this area relative to those obtained in the CB. The orientations of the null measurements, which are parallel or

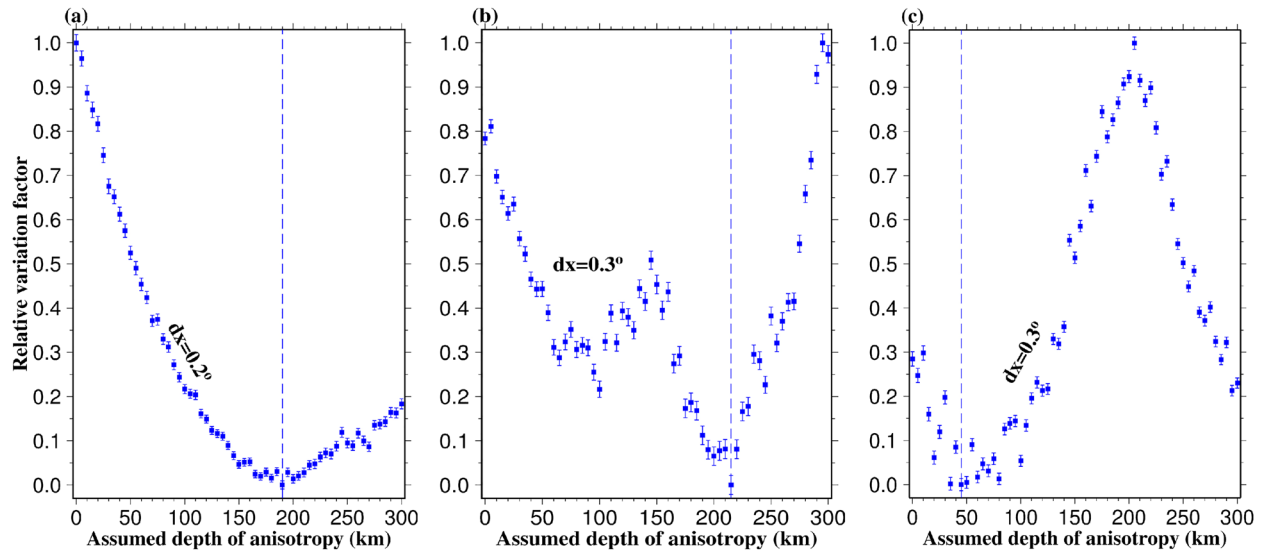


**Figure 6.** Normalized spatial variation factors computed using individual shear wave splitting measurements in areas (a) east of longitude 96.3°E in the Shan Plateau, (b) between longitudes 94°E and 95.5°E in the Central Basin, and (c) near the Sagaing Fault. The resulting optimal depth of the anisotropic layer is marked by the dashed blue line, corresponding to the minimum variation factor. Note that  $dx$  is the block size in degrees.

orthogonal to the back azimuth of the events, observed in this and the other areas are generally consistent with the fast or slow orientations (Figure S1). Note that when the well-defined and null measurements are plotted at the same depth (e.g., 200 km), for a given area both types of measurements may coexist (Figures 5a and S1b). This apparently counterintuitive phenomenon is due to the fact that the events that produced the null measurements have a back azimuth that is parallel or orthogonal to the fast orientation in the area and is not indicative of a lack of azimuthal anisotropy in the area.

## 4. Discussion

### 4.1. Estimation of the Depth of Anisotropy

To estimate the depth of the main contributing layer of the observed anisotropy, we applied the spatial coherency technique, which is reliable for areas dominated by a single layer but spatially varying azimuthal anisotropy (K. H. Liu & Gao, 2011). This technique is also applicable to the special two-layer situation when the fast orientations of the two layers are approximately orthogonal to each other. In this case, the two-layered structure is equivalent to a single layer with a fast orientation that is the same as that of the layer with the greater splitting time, and with a splitting time that is the difference between that of the two layers (Silver & Savage, 1994). For the SP (the area east of 96.3°E), the resulting optimal depth of the anisotropic layer is 190 km (Figure 6a), and in the CB (longitude range 94.0–95.5°E), the estimated depth is about 215 km (Figure 6b). Near the SF, the optimal depth is about 45 km and there is another minimum value probably corresponding to a deeper layer (Figure 6c). A dominant minimum variation factor was not found using data recorded in the IBR, probably due to the insignificant spatial variations of the splitting parameters, or due to significant variations of the depth of the anisotropic layer.

Under the assumption that the estimated lithospheric thicknesses in LITHO1.0 (Figure 7b; Pasyanos et al., 2014) are realistic, which show a thickness of  $\sim 50$  km in the SP including the area along the SF, the resultant optimal depth of 190 km for the SP suggests that the observed anisotropy is from the asthenosphere. In the vicinity of the SF, the 45 km optimal depth suggests that the anisotropy is mostly located in the lithosphere or the rheological transition zone between the lithosphere and the asthenosphere (Conrad & Behn, 2010; McKenzie, 1979; Yang et al., 2017). For this area, while the possibility that lithospheric fabrics are the main source of the observed azimuthal anisotropy cannot be completely excluded, the fact that the expected increase in the observed splitting times near the SF is not observed, suggests limited contributions from lithospheric fabrics associated with the major fault zone, where lithospheric deformation and strain

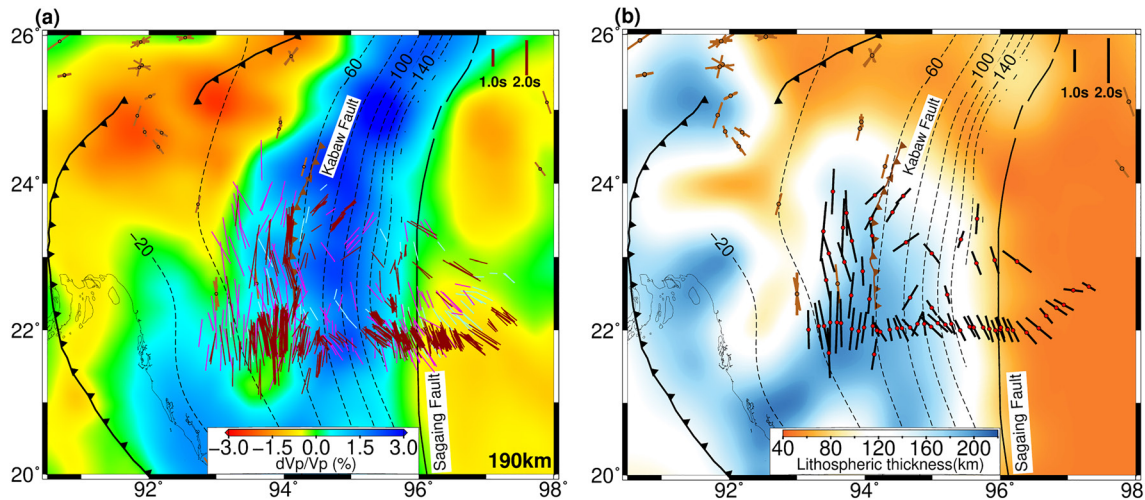


**Figure 7.** (a) Shear wave splitting measurements plotted on P-wave velocity anomalies at 190 km deep constrained from teleseismic tomography (Koulakov, 2011). Individual SKS, SKKS, and PKS measurements from this study are shown in red, purple, and blue respectively, and are plotted above the ray-piercing points at 200 km deep. Measurements from previous studies (orange bars and circles) are plotted at the station locations. (b) Station-averaged XKS splitting measurements from this study (black bars and red circles). The background image shows the thickness of the lithosphere (Pasyanos et al., 2014).

localization are the most intensive. In this area, it appears that there is a second minimum in the variation factor curve (Figure 6c) that is indicative of a layer of anisotropy in the asthenosphere. An alternative model is that the mostly N-S oriented anisotropy in the vicinity of the SF is the result of two competing layers: a shallow layer in the lithosphere with an N-S oriented anisotropy, and a deeper layer with an E-W anisotropy and a relatively smaller splitting time. Additional studies such as anisotropic surface wave tomography or full waveform modeling are needed to distinguish these models. For the central and western parts of the CB, where the top of the subducting slab has a depth ranging from 60 to 150 km (Figure 5), the estimated depth of anisotropy (~215 km) implies that the observed seismic anisotropy is most likely from the sub-slab mantle.

#### 4.2. Contribution of Lithospheric Fabrics to the Observed Anisotropy on the IBR

Lithospheric anisotropy with fast orientations perpendicular to the shortening direction can result from coherent deformation of the lithosphere (Silver, 1996; Silver & Chan, 1991). In the IBR, which was mostly the result of intensive E-W compression associated with the convergent margin (Mon et al., 2020), the fast orientations are parallel to the strike of the orogen, and the corresponding splitting times are large ( $2.09 \pm 0.55$  s on average) and are positively correlated with the topography (Figure 5d). Such a correspondence between topography (which is a measure of lithospheric compressional strain in the IBR) and the splitting times suggests possible contributions from the lithosphere of the overriding plate (Figure 8).

Beneath the stations on the IBR, the Indian slab has a depth range of about 40–60 km (Figure 1b) which is comparable to the thickness of the crust of the overriding plate (Zheng et al., 2020). Contributions from the crust can be estimated by fitting the azimuthal moveout of the P-to-S conversions from the Moho (Pms) on the RFs using a sinusoidal function (Kong et al., 2016). Clear azimuthal variations of the moveout of the Pms phase were observed at most stations on the IBR, but due to the limited back azimuthal coverage, we were only able to obtain reliable results at Station M09 (Figures 5b and S3). However, as demonstrated by Station N16 (Figures 5b and S4), the moveout of the RFs recorded at most stations with a comparable number of high-quality RFs as Station N16 on the IBR can be satisfactorily matched by the theoretical moveout curves computed using the optimal crustal anisotropy parameters obtained at M09, suggesting that results obtained at M09 are representative for crustal anisotropy in the IBR. The resulting fast orientation of crustal anisotropy is  $-9.8^\circ$  and is consistent with that obtained by the XKS splitting analysis in the same area (Figure 5b). The crustal  $\delta t$  value of 0.62 s is about 1/3 of the average XKS splitting time on the IBR and is comparable to other continental areas that are being actively thickened such as the eastern Tibetan Plateau (Kong et al., 2016). While the possibility that the contributions from a tilting Moho to the moveout

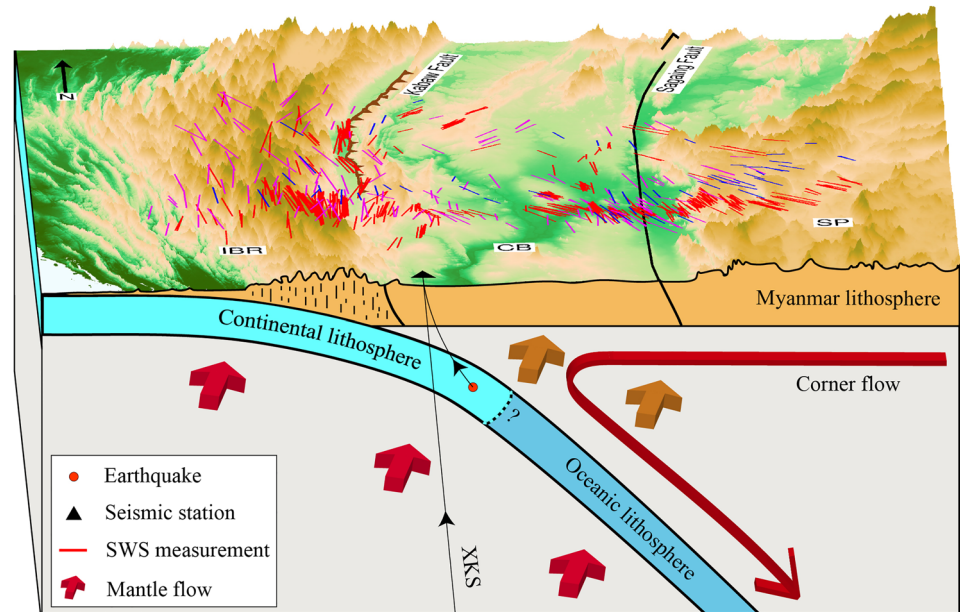


**Figure 8.** A schematic diagram showing the deformation systems that can explain the vast majority of the splitting measurements in the study area. The subducting Indian continental and oceanic slabs are shown in light blue and dark blue, respectively (Koulakov, 2011; Zheng et al., 2020). Short black lines in the Indo-Burma Ranges (IBR) indicate lithospheric fabrics associated with E-W shortening. The red and orange arrows indicate trench-parallel mantle flow in the sub-slab region and the mantle wedge, respectively. Note that the flow directions have a 180° ambiguity.

cannot be completely excluded, the fact that the arrival time of the Pms from events from the west (~270° back-azimuth), which sample thinner crust, is relatively late at both stations shown in Figures S3 and S4, suggests limited contributions from an eastward tilting Moho.

### 4.3. Mantle Wedge Anisotropy Beneath the CB Revealed by Splitting of Local S-Waves

To estimate the contribution of the mantle wedge beneath the CB to the observed XKS splitting, we conducted splitting analysis using S-waves originated from local earthquakes in the S-wave window (see Figure S5 for examples) which is defined by a maximum incident angle of about 35° (Booth & Crampin, 1985). The seismograms were band-pass filtered in the frequency band of 0.1–1 Hz. We obtained 20 pairs of well-defined SWS parameters from 9 events with a focal depth ranging from 50 to 160 km (Figure S6). The splitting times range from 0.12 to 0.6 s with a mean value of  $0.39 \pm 0.12$  s, which is about 1/3 of the average XKS splitting time in the CB. The fast orientations from the local S-waves are mostly N-S, but a few of them are nearly E-W, resulting in a bimodal distribution, as indicated by the rose diagram in Figure 5b. The splitting parameters and information of the events for the local S splitting measurements can be found at [ftp://159.226.119.161/data/CMGSMO-1/SWSData/web\\_localS/all/web\\_localS.html](ftp://159.226.119.161/data/CMGSMO-1/SWSData/web_localS/all/web_localS.html) (Internet Explorer is recommended to open the link).

A recent study suggests that the earthquakes used for the local S splitting analysis mainly concentrate in the lower part of the subducting crust (Zheng et al., 2020). Therefore, the anisotropy responsible for the observed local S splitting parameters must reside in the mantle wedge, the overriding plate, or the slab. The fact that different splitting measurements using different local S events were observed at the same stations (e.g., Stations E06 and M13 in Figure S6) implies that the overriding plate, in which the rays from different events coming to the same station sample similar areas, is not the main source of the observed anisotropy. Similarly, the fact that different splitting parameters were observed using data from the same events (e.g., event 2017-346-05:56, i.e., light blue star in Figure S6) recorded by different stations suggests that the subducting slab, in which the rays to different stations sample similar areas, is also not the main source of anisotropy. Therefore, we infer that the anisotropy observed from local earthquakes mainly comes from the mantle wedge.

In the mantle wedge beneath the western part of the CB, a low shear-wave velocity zone has recently been imaged at a depth of  $\sim 40$  km (Wu et al., 2021). Additionally, P-wave and S-wave velocities at the nose of the mantle wedge below the CB are basically consistent with the velocities in the thicker portions of the mantle wedge (Zhang et al., 2021), suggesting that the nose of the mantle wedge is not particularly cold. We speculate that the bimodal distribution of the fast orientations observed using local S-waves in the CB (Figure 5b) may mainly arise from two flow systems with nearly orthogonal directions (Figure 8). Under the assumption that the previously suggested slab tear at  $21^\circ\text{N}$  (Bai et al., 2020) and slab gap at  $\sim 26^\circ\text{N}$  (Raouf et al., 2017) do exist, we propose that the sub-slab mantle is transported through the slab tear or gap into the mantle wedge, forming the trench-parallel flow system. This kind of transportation of sub-slab materials through a slab gap into the mantle wedge has been suggested by both numerical modeling (e.g., Jadamec, 2016; Király et al., 2020) and observation studies (e.g., Kong et al., 2020). The second flow is the horizontal component of a two-dimensional corner flow system in the mantle wedge associated with viscous coupling between the slab and the overlying mantle (C. E. Hall et al., 2000), resulting in trench-perpendicular fast orientations. It has long been recognized that for two anisotropy forming processes with orthogonal fast orientations, the net splitting time is the difference of the individual splitting time of the two processes, and the fast orientation is the same as that having the greater splitting time (Silver & Savage, 1994). Therefore, depending on which of the two flow systems has a greater strength in a given region in the CB, the resulting net fast orientation revealed by local S-wave splitting analysis could either be N-S if the trench parallel flow dominates, or E-W if the corner flow dominates (Figure 8).

An alternative interpretation is that the overall flow field in the mantle wedge is trench-parallel, but contributions from E-W oriented anisotropy in the slab or the overriding plate complicate this pattern, resulting in sporadic E-W fast orientations when the splitting time associated with the E-W anisotropy is greater than that from the trench-parallel flow. Because most crustal earthquakes in the CB show nearly N-S striking dextral strike-slip (Mon et al., 2020), which will most likely induce N-S oriented anisotropy, at least the crustal portion of the overriding plate is unlikely to be a main contributor to the E-W anisotropy. For the subducting slab, it may preserve the approximately E-W oriented fossilized fabric from the time of plate formation at the mid-ocean ridge (Francis, 1969; Hess, 1964). Because it is unclear whether such fabric is preserved or overprinted during the slab subduction, its contribution to the observed anisotropy cannot be reliably quantified.

#### 4.4. Trench-Perpendicular Corner Flow Beneath the SP

The fast orientations observed in the SP using XKS show a clear transition from nearly N-S along the SF to NW-SE and WNW-ESE in the eastern portion of this region, implying a gradual transition from trench-parallel dominated flow system to trench-perpendicular flow system (Figure 8). The WNW-ESE fast orientations are similar to the ones observed in the SE Tibetan Plateau (Huang et al., 2015) and the Indochina Peninsula (Yu et al., 2018) located to the NE and east, respectively, of the study area. The trench-perpendicular fast orientations away from the trench can be well explained by a corner flow system (Figure 8) induced by the subduction of the Indian Plate.

#### 4.5. Implications on Sub-Slab Mantle Flow

Previously determined fast orientations in the Indian Plate mostly coincide with the NE-SW absolute plate motion (APM) direction, implying simple shear at the base of the lithosphere is the dominant mechanism for forging anisotropy (Roy et al., 2014; L. Liu et al., 2019). However, the fast orientations observed in central Myanmar are inconsistent with the APM direction of the Indian Plate. Hypocentral relocations and seismic tomography studies have revealed a systematic lateral variation in the strike of the subducted slab beneath the CB (Figure 7a; Hurukawa et al., 2012; Koulakov, 2011), which is consistent with the spatial variation of the fast orientations from NNW-SSE in the south to NNE-SSW in the north. The subducting Indian Plate is undergoing westward slab rollback (Kundu & Gahalaut, 2012; Lee et al., 2016; Sternai et al., 2016) and trench retreat (R. Hall & Morley, 2004; Kundu & Gahalaut, 2012; Li et al., 2008), forcing the sub-slab mantle to flow parallel along the slab (Becker & Faccenna, 2009; Long & Silver, 2008) and providing a viable mechanism for the correspondence between the observed fast orientations and the trend of the subducted slab observed in the CB.

Finally, the anomalously high splitting times observed in the IBR can readily be interpreted as the combined results of N-S oriented sub-slab flow and N-S oriented, compression-induced lithospheric fabrics in the overriding plate (Figure 8). Similarly, the sudden drop in the splitting times at the IBR/CB boundary and the close correspondence between the splitting times and the elevation (Figure 5d) can also be explained by the rapid eastward reduction of the compression-induced lithospheric strain at the eastern edge of the IBR.

## 5. Conclusions

In this study, we employed a newly recorded broadband seismic data set to conduct the first regional-scale SWS investigation of central Myanmar, an area that is dominated by oblique subduction. The resulting splitting parameters reveal systematic spatial variations of mantle anisotropy that can be attributed to three flow systems driven by slab rollback and subduction. Spatial coherency analysis of the splitting parameters, large splitting times in the IBR, and crustal anisotropy analyses suggest that the source of the referred anisotropy is mostly located in the sub-slab mantle beneath the IBR and CB, and in the upper asthenosphere beneath the SP. N-S crustal anisotropy resulting from the lithospheric shortening of the overriding plate contributes significantly to the anomalously large splitting times observed on the IBR, and the rest is from sub-slab trench parallel flow. Beneath the CB, most of the fast orientations obtained using S-waves from local events located along the subducted slab show either N-S or E-W fast orientations with small splitting times, which can be attributed to variations in the relative strength of the E-W oriented corner flow induced by slab subduction and the N-S oriented trench parallel flow that is driven by slab rollback and enters the mantle wedge from a tomographically revealed slab gap or a slab tear. Spatially varying XKS splitting parameters in the SP can be explained by a model involving eastward diminishing trench-parallel flow systems and the E-W oriented corner flow that affects the eastern SP and most parts of the Indochina Peninsula and SE Tibetan Plateau.

## Data Availability Statement

Data used in this study were provided by the Seismic Array Laboratory at the Institute of Geology and Geophysics, Chinese Academy of Sciences (IGGCAS).

## Acknowledgments

We are grateful to all the participants in the CMGSMO project for installing and maintaining the seismic network. The CMGSMO teleseismic waveform data, local earthquake waveform data, and receiver function data used in this study can be accessed from <http://www.geophys.ac.cn/ArticleDataInfo.asp?MetaId=309>. Most figures were plotted by the Generic Mapping Tools (GMT; Wessel et al., 2013). This study is supported by National Natural Science Foundation of China (grants 91755214, 42030309, and 41490612). E. F. is supported by a scholarship provided by the University of Chinese Academy of Sciences (UCAS). The data analysis component is partially supported by the United States National Science Foundation under awards 1830644 and 1919789.

## References

- Ando, M., Ishikawa, Y., & Wada, H. (1980). S-wave anisotropy in the upper mantle under a volcanic area in Japan. *Nature*, 286(5768), 43–46. <https://doi.org/10.1038/286043a0>
- Argus, D. F., Gordon, R. G., & DeMets, C. (2011). Geologically current motion of 56 plates relative to the no-net-rotation reference frame. *Geochemistry, Geophysics, Geosystems*, 12(11), Q11001. <https://doi.org/10.1029/2011gc003751>
- Bai, Y., Yuan, X., He, Y., Hou, G., Thant, M., Sein, K., & Ai, Y. (2020). Mantle transition zone structure beneath Myanmar and its geodynamic implications. *Geochemistry, Geophysics, Geosystems*, 21(12), e2020GC009262. <https://doi.org/10.1029/2020gc009262>
- Becker, T. W., & Faccenna, C. (2009). A review of the role of subduction dynamics for regional and global plate motions. In S. Lallemand, & F. Funiciello (Eds.), *Subduction zone geodynamics* (pp. 3–34). Berlin: Springer. [https://doi.org/10.1007/978-3-540-87974-9\\_1](https://doi.org/10.1007/978-3-540-87974-9_1)
- Booth, D. C., & Crampin, S. (1985). Shear-wave polarizations on a curved wavefront at an isotropic free surface. *Geophysical Journal of the Royal Astronomical Society*, 83(1), 31–45. <https://doi.org/10.1111/j.1365-246X.1985.tb05154.x>
- Conrad, C. P., & Behn, M. D. (2010). Constraints on lithosphere net rotation and asthenospheric viscosity from global mantle flow models and seismic anisotropy. *Geochemistry, Geophysics, Geosystems*, 11(5), Q05W05. <https://doi.org/10.1029/2009GC002970>
- Crampin, S., & Booth, D. C. (1985). Shear-wave polarizations near the North Anatolian Fault—II. Interpretation in terms of crack-induced anisotropy. *Geophysical Journal International*, 83(1), 75–92. <https://doi.org/10.1111/j.1365-246X.1985.tb05157.x>
- Curry, J. R. (2005). Tectonics and history of the Andaman Sea region. *Journal of Asian Earth Sciences*, 25(1), 187–232. <https://doi.org/10.1016/j.jseas.2004.09.001>
- Francis, T. J. G. (1969). Generation of seismic anisotropy in the upper mantle along the mid-oceanic ridges. *Nature*, 221(5176), 162–165. <https://doi.org/10.1038/221162b0>
- Frohlich, C. (2006). *Deep earthquakes*. Cambridge University Press.
- Hall, C. E., Fischer, K. M., Parmentier, E. M., & Blackman, D. K. (2000). The influence of plate motions on three-dimensional back arc mantle flow and shear wave splitting. *Journal of Geophysical Research*, 105(B12), 28009–28033. <https://doi.org/10.1029/2000JB900297>
- Hall, R., & Morley, C. K. (2004). Sundaland basins. In P. Clift, P. Wang, W. Kuhnt, & D. Hayes (Eds.), *Continent-ocean interactions within east Asian marginal seas* (pp. 55–85). Washington: Geophysical Monograph Series. <https://doi.org/10.1029/149gm04>
- Hayes, G. P., Moore, G. L., Portner, D. E., Hearne, M., Flamme, H., Furtney, M., & Smoczyk, G. M. (2018). Slab2, a comprehensive subduction zone geometry model. *Science*, 362(6410), 58–61. <https://doi.org/10.1126/science.aat4723>
- Hess, H. H. (1964). Seismic anisotropy of the uppermost mantle under oceans. *Nature*, 203(4945), 629–631. <https://doi.org/10.1038/203629a0>
- Huang, Z., Wang, L., Xu, M., Ding, Z., Wu, Y., Wang, P., et al. (2015). Teleseismic shear-wave splitting in SE Tibet: Insight into complex crust and upper-mantle deformation. *Earth and Planetary Science Letters*, 432, 354–362. <https://doi.org/10.1016/j.epsl.2015.10.027>

- Hurukawa, N., Tun, P. P., & Shibazaki, B. (2012). Detailed geometry of the subducting Indian Plate beneath the Burma Plate and sub-crustal seismicity in the Burma Plate derived from joint hypocenter relocation. *Earth Planets and Space*, 64(4), 333–343. <https://doi.org/10.5047/eps.2011.10.011>
- Jadamec, M. A. (2016). Insights on slab-driven mantle flow from advances in three-dimensional modelling. *Journal of Geodynamics*, 100, 51–70. <https://doi.org/10.1016/j.jog.2016.07.004>
- Jung, H., & Karato, S.-I. (2001). Water-induced fabric transitions in olivine. *Science*, 293(5534), 1460–1463. <https://doi.org/10.1126/science.1062235>
- Karato, S.-I., Jung, H., Katayama, I., & Skemer, P. (2008). Geodynamic significance of seismic anisotropy of the upper mantle: New insights from laboratory studies. *Annual Review of Earth and Planetary Sciences*, 36(1), 59–95. <https://doi.org/10.1146/annurev.earth.36.031207.124120>
- Király, Á., Portner, D. E., Haynie, K. L., Chilson-Parks, B. H., Ghosh, T., Jadamec, M., et al. (2020). The effect of slab gaps on subduction dynamics and mantle upwelling. *Tectonophysics*, 785, 228458. <https://doi.org/10.1016/j.tecto.2020.228458>
- Kong, F., Gao, S. S., Liu, K. H., Zhang, J., & Li, J. (2020). Seismic anisotropy and mantle flow in the Sumatra subduction zone constrained by shear wave splitting and receiver function analyses. *Geochemistry, Geophysics, Geosystems*, 21(2), e2019GC008766. <https://doi.org/10.1029/2019gc008766>
- Kong, F., Wu, J., Liu, K. H., & Gao, S. S. (2016). Crustal anisotropy and ductile flow beneath the eastern Tibetan Plateau and adjacent areas. *Earth and Planetary Science Letters*, 442, 72–79. <https://doi.org/10.1016/j.epsl.2016.03.003>
- Koulakov, I. (2011). High-frequency P and S velocity anomalies in the upper mantle beneath Asia from inversion of worldwide traveltimes. *Journal of Geophysical Research*, 116(B4), B04301. <https://doi.org/10.1029/2010jb007938>
- Kundu, B., & Gahalaut, V. K. (2012). Earthquake occurrence processes in the Indo-Burmese wedge and Sagaing fault region. *Tectonophysics*, 524–525, 135–146. <https://doi.org/10.1016/j.tecto.2011.12.031>
- Lee, H.-Y., Chung, S.-L., & Yang, H.-M. (2016). Late Cenozoic volcanism in central Myanmar: Geochemical characteristics and geodynamic significance. *Lithos*, 245, 174–190. <https://doi.org/10.1016/j.lithos.2015.09.018>
- Li, C., van der Hilst, R. D., Meltzer, A. S., & Engdahl, E. R. (2008). Subduction of the Indian lithosphere beneath the Tibetan Plateau and Burma. *Earth and Planetary Science Letters*, 274(1–2), 157–168. <https://doi.org/10.1016/j.epsl.2008.07.016>
- Liu, K. H., & Gao, S. S. (2011). Estimation of the depth of anisotropy using spatial coherency of shear-wave splitting parameters. *Bulletin of the Seismological Society of America*, 101(5), 2153–2161. <https://doi.org/10.1785/0120100258>
- Liu, K. H., & Gao, S. S. (2013). Making reliable shear-wave splitting measurements. *Bulletin of the Seismological Society of America*, 103(5), 2680–2693. <https://doi.org/10.1785/0120120355>
- Liu, K. H., Gao, S. S., Gao, Y., & Wu, J. (2008). Shear wave splitting and mantle flow associated with the deflected Pacific slab beneath northeast Asia. *Journal of Geophysical Research*, 113(B1), B01305. <https://doi.org/10.1029/2007jb005178>
- Liu, L., Gao, S. S., Liu, K. H., Li, S., Tong, S., & Kong, F. (2019). Toroidal mantle flow induced by slab subduction and rollback beneath the eastern Himalayan syntaxis and adjacent areas. *Geophysical Research Letters*, 46(20), 11080–11090. <https://doi.org/10.1029/2019gl084961>
- Long, M. D., & Silver, P. G. (2008). The subduction zone flow field from seismic anisotropy: A global view. *Science*, 319(5861), 315–318. <https://doi.org/10.1126/science.1150809>
- Mallick, R., Lindsey, E. O., Feng, L., Hubbard, J., Banerjee, P., & Hill, E. M. (2019). Active convergence of the India-Burma-Sunda plates revealed by a new continuous GPS network. *Journal of Geophysical Research: Solid Earth*, 124(3), 3155–3171. <https://doi.org/10.1029/2018jb016480>
- McCormack, K., Wirth, E. A., & Long, M. D. (2013). B-type olivine fabric and mantle wedge serpentinization beneath the Ryukyu arc. *Geophysical Research Letters*, 40(9), 1697–1702. <https://doi.org/10.1002/grl.50369>
- McKenzie, D. (1979). Finite deformation during fluid flow. *Geophysical Journal of the Royal Astronomical Society*, 58(3), 689–715. <https://doi.org/10.1111/j.1365-246X.1979.tb04803.x>
- Mitchell, A. H. G. (1989). The Shan Plateau and western Burma: Mesozoic-cenozoic plate boundaries and correlations with Tibet. In A. M. C. Şengör (Ed.), *Tectonic evolution of the Tethyan region* (pp. 567–583). Dordrecht: Springer Netherlands. [https://doi.org/10.1007/978-94-009-2253-2\\_24](https://doi.org/10.1007/978-94-009-2253-2_24)
- Mon, C. T., Gong, X., Wen, Y., Jiang, M., Chen, Q. F., Zhang, M., et al. (2020). Insight into major active faults in central Myanmar and the related geodynamic sources. *Geophysical Research Letters*, 47(8), e2019GL086236. <https://doi.org/10.1029/2019gl086236>
- Pasyanos, M. E., Masters, T. G., Laske, G., & Ma, Z. (2014). LITHO1.0: An updated crust and lithospheric model of the Earth. *Journal of Geophysical Research: Solid Earth*, 119(3), 2153–2173. <https://doi.org/10.1002/2013jb010626>
- Rangin, C. (2017). Active and recent tectonics of the Burma Platelet in Myanmar. *Geological Society, London, Memoirs*, 48(1), 53–64. <https://doi.org/10.1144/M48.3>
- Raouf, J., Mukhopadhyay, S., Koulakov, I., & Kayal, J. R. (2017). 3-D seismic tomography of the lithosphere and its geodynamic implications beneath the northeast India region. *Tectonics*, 36(5), 962–980. <https://doi.org/10.1002/2016tc004375>
- Roy, S. K., Kumar, M. R., & Srinagesh, D. (2014). Upper and lower mantle anisotropy inferred from comprehensive SKS and SKKS splitting measurements from India. *Earth and Planetary Science Letters*, 392, 192–206. <https://doi.org/10.1016/j.epsl.2014.02.012>
- Rümpker, G., & Silver, P. G. (1998). Apparent shear-wave splitting parameters in the presence of vertically varying anisotropy. *Geophysical Journal International*, 135(3), 790–800. <https://doi.org/10.1046/j.1365-246X.1998.00660.x>
- Russo, R. M. (2012). Source-side shear-wave splitting and upper-mantle flow beneath the Arakan slab, India-Asia-Sundaland triple junction. *Geosphere*, 8(1), 158–178. <https://doi.org/10.1130/ges00534.1>
- Saikia, D., Kumar, M. R., Singh, A., Roy, S. K., Raju, P. S., & Lyngdoh, A. C. (2018). Mantle deformation in the eastern Himalaya, Burmese arc and adjoining regions. *Geochemistry, Geophysics, Geosystems*, 19(11), 4420–4432. <https://doi.org/10.1029/2018gc007691>
- Silver, P. G. (1996). Seismic anisotropy beneath the continents: Probing the depths of geology. *Annual Review of Earth and Planetary Sciences*, 24(1), 385–432. <https://doi.org/10.1146/annurev.earth.24.1.385>
- Silver, P. G., & Chan, W. W. (1991). Shear wave splitting and subcontinental mantle deformation. *Journal of Geophysical Research*, 96(B10), 16429–16454. <https://doi.org/10.1029/91jb00899>
- Silver, P. G., & Savage, M. K. (1994). The interpretation of shear-wave splitting parameters in the presence of two anisotropic layers. *Geophysical Journal International*, 119(3), 949–963. <https://doi.org/10.1111/j.1365-246X.1994.tb04027.x>
- Sloan, R. A., Elliott, J. R., Searle, M. P., & Morley, C. K. (2017). Chapter 2: Active tectonics of Myanmar and the Andaman Sea. *Geological Society, London, Memoirs*, 48(1), 19–52. <https://doi.org/10.1144/M48.2>
- Steckler, M. S., Mondal, D. R., Akhter, S. H., Seiber, L., Feng, L., Gale, J., et al. (2016). Locked and loading megathrust linked to active subduction beneath the Indo-Burman Ranges. *Nature Geoscience*, 9(8), 615–618. <https://doi.org/10.1038/ngeo2760>

- Sternai, P., Avouac, J.-P., Jolivet, L., Faccenna, C., Gerya, T., Becker, T. W., & Menant, A. (2016). On the influence of the asthenospheric flow on the tectonics and topography at a collision-subduction transition zones: Comparison with the eastern Tibetan margin. *Journal of Geodynamics*, *100*, 184–197. <https://doi.org/10.1016/j.jog.2016.02.009>
- Wang, M., & Shen, Z. K. (2020). Present-day crustal deformation of continental China derived from GPS and its tectonic implications. *Journal of Geophysical Research: Solid Earth*, *125*(2), e2019JB018774. <https://doi.org/10.1029/2019jb018774>
- Wang, Y., Sieh, K., Tun, S. T., Lai, K.-Y., & Myint, T. (2014). Active tectonics and earthquake potential of the Myanmar region. *Journal of Geophysical Research: Solid Earth*, *119*(4), 3767–3822. <https://doi.org/10.1002/2013jb010762>
- Wessel, P., Smith, W. H. F., Scharroo, R., Luis, J., & Wobbe, F. (2013). Generic mapping tools: Improved version released. *Eos, Transactions American Geophysical Union*, *94*(45), 409–410. <https://doi.org/10.1002/2013EO450001>
- Wu, S., Yao, J., Wei, S., Hubbard, J., Wang, Y., Min Htwe, Y. M., et al. (2021). New insights into the structural heterogeneity and geodynamics of the Indo-Burma subduction zone from ambient noise tomography. *Earth and Planetary Science Letters*, *562*, 116856. <https://doi.org/10.1016/j.epsl.2021.116856>
- Yang, B. B., Liu, Y., Dahm, H., Liu, K. H., & Gao, S. S. (2017). Seismic azimuthal anisotropy beneath the eastern United States and its geodynamic implications. *Geophysical Research Letters*, *44*(6), 2670–2678. <https://doi.org/10.1002/2016GL071227>
- Yao, J., Liu, S., Wei, S., Hubbard, J., Huang, B. S., Chen, M., & Tong, P. (2021). Slab models beneath central Myanmar revealed by a joint inversion of regional and teleseismic traveltimes. *Journal of Geophysical Research: Solid Earth*, *126*(2), e2020JB020164. <https://doi.org/10.1029/2020jb020164>
- Yu, Y., Gao, S. S., Liu, K. H., Yang, T., Xue, M., Le, K. P., & Gao, J. (2018). Characteristics of the mantle flow system beneath the Indochina Peninsula revealed by teleseismic shear wave splitting analysis. *Geochemistry, Geophysics, Geosystems*, *19*, 1519–1532. <https://doi.org/10.1029/2018GC007474>
- Zhang, G., He, Y., Ai, Y., Jiang, M., Mon, C. T., Hou, G., et al. (2021). Indian continental lithosphere and related volcanism beneath Myanmar: Constraints from local earthquake tomography. *Earth and Planetary Science Letters*, *567*, 116987. <https://doi.org/10.1016/j.epsl.2021.116987>
- Zheng, T., He, Y., Ding, L., Jiang, M., Ai, Y., Mon, C. T., et al. (2020). Direct structural evidence of Indian continental subduction beneath Myanmar. *Nature Communication*, *11*(1), 1944. <https://doi.org/10.1038/s41467-020-15746-3>